Available online at www.sciencedirect.com
SCIENCE DIRECT®

NUCLEAR SCIENCE AND TECHNIQUES

Nuclear Science and Techniques, Vol.17, No.6 (2006) 342–353

Principle of diffraction enhanced imaging (DEI) and computed tomography based on DEI method

ZHU Pei-Ping[1] HUANG Wan-Xia[1] YUAN Qing-Xi[1] YU Jian[2] WANG Jun-Yue[1]
ZHENG Xin[1] SHU Hang[1] CHEN Bo[1] LIU Yi-Jin[1] LI En-Rong[1] WU Zi-Yu[1]

([1] Beijing Synchrotron Radiation Facility, Institute of High Energy Physics,
Chinese Academy of Sciences, Beijing 100049, China;
[2] Electronic Institute of Dalian University of Technology, Dalian 116023, China)

Abstract In the first part of this article a more general DEI equation was derived using simple concepts. Not only does the new DEI equation explain all the problems that can be done by the DEI equation proposed by Chapman, but also explains the problem that can not be explained with the old DEI equation, such as the noise background caused by the small angle scattering reflected by the analyzer. In the second part, a DEI-PI-CT formula has been proposed and the contour contrast caused by the extinction of refraction beam has been qualitatively explained, and then based on the work of Ando's group two formulae of refraction CT with DEI method has been proposed. Combining one refraction CT formula proposed by Dilmanian with the two refraction CT formulae proposed by us, the whole framework of CT algorithm can be made to reconstruct three components of the gradient of refractive index.

Key words Diffraction enhanced imaging, Refraction computed tomography, Synchrotron radiation

CLC numbers O434.14, TH774

Part I. Diffraction enhanced imaging (DEI)

1 Introduction

The DEI is one of the three or four main kinds of phase contrast imaging[1-9], because of the simpler mathematic description proposed by Chapman and his coworkers[6] in 1997, and it has been widely accepted and applied by scientists in medical, biological, material and other fields. The essence of DEI is using diffraction of perfect crystals to suppress certain angular information and enhance the rest. For example, the DEI pays attention to the angular information in meridian plane and ignores that in sagittal plane; another example, the refraction image in DEI suppresses absorption and scattering information and enhances the refraction information, and so on. The DEI can employ one of three contrast mechanisms or combine them together to enhance greatly the contrast of the image. It is certainly one of the most effective X-ray phase contrast imaging methods, which shows significant advantages when compared to the conventional X-ray absorption imaging techniques, widely applied to the investigation of biological and medical systems. The DEI equation[6]

$$I = I_{\mathrm{R}} R(\theta_{\mathrm{A}} + \theta_{\mathrm{m}}) \tag{1}$$

was proposed by Chapman and co-workers, where I_{R} written in implicit form represents the decay of the photon beam induced by absorption inside the sample and extinction (i.e. rejection of the small angle scat-

Supported by the National Outstanding Youth Fund (10125523 to Z.Wu.), the Key Important Nano-Research Project (90206032), the Key Important Project of the National Natural Science Foundation of China (10490190, 10490194) and by Knowledge Innovation Fund of IHEP.

Email: zhupp@mail.ihep.ac.cn.

tering) by the analyzer crystal, θ_A is the setting angle of the analyzer, while θ_m is the refraction angle in the meridian plane. The equation has been widely accepted and used by scientists in biological, medical and other fields. However, in this equation the part of the small angle scattering reflected by the analyzer crystal is neglected, and there is no explicit expression to describe the influence of small angle scattering on imaging. In the following the more general DEI equation is derived using certain simple concepts and mathematics at first, and then some new results are discussed by using the new DEI equation.

2 Derivation of more general DEI equation

2.1 The method to study imaging

The theory for imaging is about the relation between the image and object, its purpose is to get better images with high resolution and high contrast. The method to study imaging is to choose an object point on the object plane, and then to study its corresponding image point. If the relation between an object point and its corresponding image point is made out, the quality of the image can be predicted. The more general DEI equation will be derived in the same way.

2.2 DEI is the development from two old kinds of imaging

The DEI is a new kind of X-ray imaging method, and it can obtain much better image compared with the traditional X-ray projection imaging, but it can be treated as the development from both pinhole imaging and traditional X-ray projection imaging. Fig. 1 shows the comparison between the traditional X-ray projection image and the DEI image of a fly.

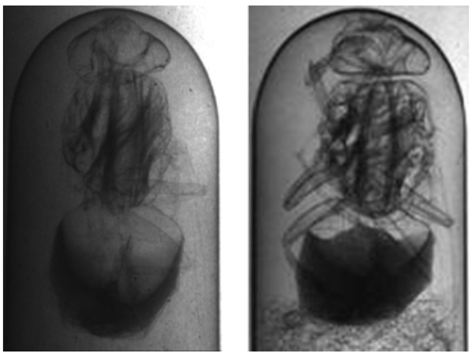

Fig.1 On the left is the traditional X-ray projection image, and on the right is the image of a fly taken with DEI method.

About 2300 years ago a Chinese ancient scientist called Mozi (墨子) pointed out the principle of pinhole imaging, as shown in Fig.2. And the first X-ray projection image was taken by a German physicist, Professor W. C. Roentgen in 1895. Fig. 3 demonstrates the relation between pinhole imaging and projection imaging. From Fig. 3, the following conclusion for projection imaging can be derived: (1) each object point experiences almost the same imaging process, and it is enough to study only one of points of the object; (2) the pinhole image of the source is the point spread function of projection imaging; (3) the smaller the source and the longer source-to-object distance are, the smaller the point spread function is, resulting in the better image.

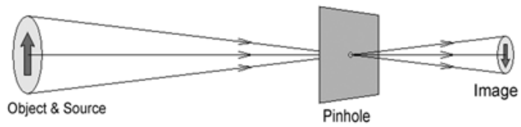

Fig.2 The principle of pinhole imaging.

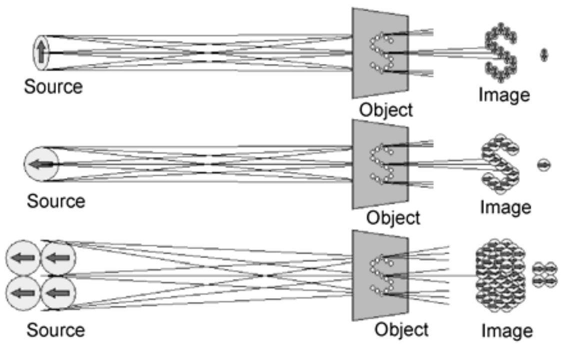

Fig.3 The smaller source and the longer distance from source to object, the better qualities the image has.

The DEI can be regarded as the projection imaging plus two perfect crystals, one of which is the monochromator and the other is the analyzer, as shown in Fig.4. Although there are several monochromatic components that go through an object point, it is enough for us to study one of them because each monochromatic component experiences almost the same imaging process. X-ray was set along the Z axis, while the X axis is perpendicular to the paper and the Y-Z plane becomes the meridional plane. Because of the property of crystal reflection[10], the perfect crystal is only sensitive to the angle in the meridional plane, and ignores that in the sagittal plane.

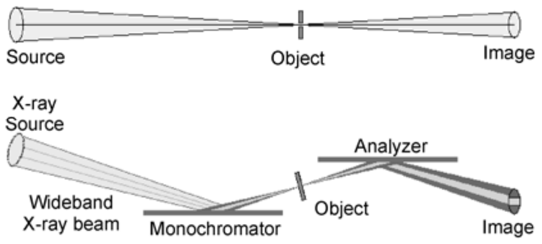

Fig.4 DEI can be regarded as the projection imaging plus two perfect crystals.

When a monochromatic component of X-rays goes through the object, it will be refracted, scattered (here only small angle scattering is considered because inelastic scattering is totally rejected by the analyzer) and absorbed. The refraction angle, extinction and absorption can be expressed respectively in the following:

$$\theta_{\mathrm{m}}(x,y)=\frac{\partial\overline{n}(x,y)}{\partial y}t(x,y)=\int_0^{t(x,y)}\frac{\partial n(x,y,z)}{\partial y}\mathrm{d}z=\sum\frac{\partial n_i}{\partial y}z_i \tag{2}$$

$$\overline{\chi}(x,y)t(x,y)=\int_0^{t(x,y)}\chi(x,y,z)\mathrm{d}z=\sum\chi_i z_i \tag{3}$$

$$\overline{\mu}(x,y)t(x,y)=\int_0^{t(x,y)}\mu(x,y,z)\mathrm{d}z=\sum\mu_i z_i \tag{4}$$

where $t(x,y)$ is the thickness of the point (x,y) of the sample, $n(x,y,z)$ is refractive index, $\chi(x,y,z)$ is extinction coefficient, and $\mu(x,y,z)$ is absorption coefficient. Three interactions are described in Fig.5 respectively.

2.3 Derivation of more general DEI equation

The more general DEI equation is derived step by step from the simple case to the complicated one[11]. At first the DEI equation is derived when the object point is a pinhole; then the DEI equation is derived when the object point can refract X-rays, following this, the DEI equation is derived when the object point can both refract and scatter X-rays; and finally the DEI equation is derived when the object point can not only refract and scatter but also absorb X-rays.

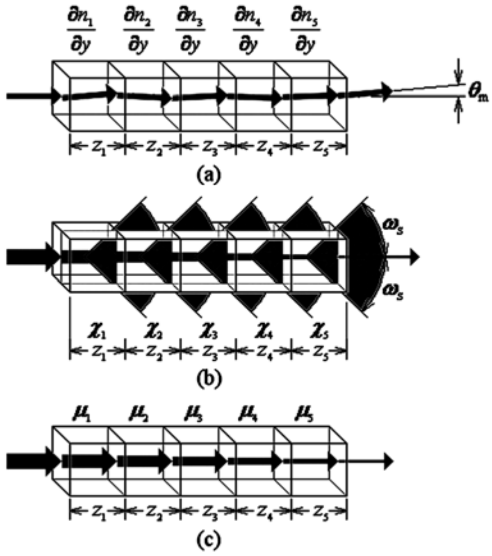

Fig.5 (a) No photon disappears in the refraction process, but all photons of the beam change their direction like one photon; (b) No photon disappears in the small angle scattering process, but most of them are scattered into relative large angular width, and a few are still in the original direction; and ω_{S} is the distribution width of small angle scattering in the meridional plane; (c) certain photons disappear in the absorption process.

When the object point (x,y) is a pinhole, there is no interaction between the object point and X-rays, the intensity on the detector is determined by the setting angle θ_{A} of the analyzer (see Fig.6). And the imaging process can be expressed as

$$I=I_0R(\theta_{\mathrm{A}}) \tag{5}$$

where $R(\theta_{\mathrm{A}})$ is the rocking curve of the monochromator-analyzer system which is mainly determined by the superposed angle of the angular width of exit beam from the pinhole and the accepted angular width of the analyzer. For the sake of simplicity and more intuitional instruction, $R(\theta_A)$ is approximately drawn as a triangle-like curve in Fig. 7.

When the object point (x,y) can refract X-rays, as if a small prism were put on the pinhole, the imaging process can be expressed as

$$I=I_0R(\theta_{\mathrm{A}}+\theta_{\mathrm{m}}) \tag{6}$$

because the refraction angle is equivalent to the setting angle of the analyzer.

When the object point (x,y) can scatter X-rays, as if a small weak scatterer were added on the pinhole, $I_0\overline{\chi}t$ is the amount scattered into the distribution with the angular width of $2\omega_{\mathrm{S}}$, the most part of $I_0\overline{\chi}t$ is rejected by the analyzer because $2\omega_{\mathrm{S}}$ is much larger than the acceptance of the analyzer, and only a very small part $I_0\bar{\chi}t\theta_D/(2\omega_S)$ goes into the acceptance of the analyzer and is reflected onto the detector by the analyzer (see Fig. 5(b)). So the imaging process can be expressed as

$$I = I_0(1-\bar{\chi}t)R(\theta_A+\theta_m)+I_0\bar{\chi}t\frac{\theta_D}{2\omega_S} \qquad (7)$$

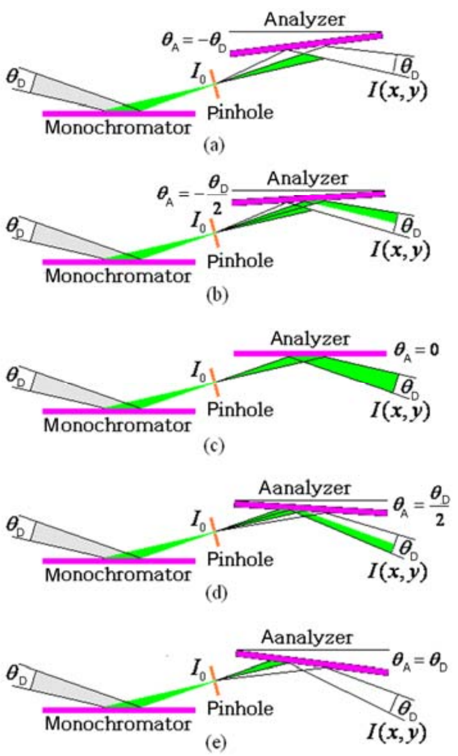

Fig.6 The reflectivity $R(\theta_A)$, called rocking curve in general, for the transmission beam going through the pinhole is the function of the setting angle θ_A of the analyzer, which is determined by the superposition angle of the angular width of the transmission beam and the acceptance of the analyzer. (a) $R(\theta_A)=0$ when $\theta_A\le-\theta_D$;(b) $R(\theta_A)=0.5$ when $\theta_A=-\theta_D/2$; (c) $R(\theta_A)=1$ when $\theta_A=0$; (d) $R(\theta_A)=0.5$ when $\theta_A=\theta_D/2$; (e) $R(\theta_A)=0$ when $\theta_A\ge\theta_D$.

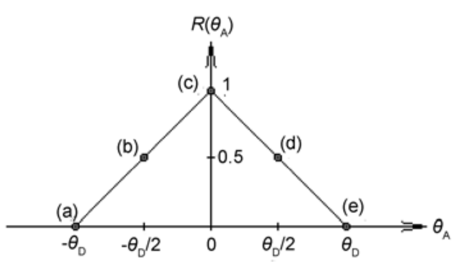

Fig.7 $R(\theta_A)$ drawn as a triangle-like curve, with five points of (a), (b), (c), (d) and (e) on the curve corresponding to the five figures of (a), (b), (c), (d), and (e) in Fig.6 respectively.

In general the object point (x,y) can not only refract and scatter, but also absorb X-rays, as if a small weak absorber were added once more on the pinhole, the remaining intensity of the not scattered X-rays after absorption is $I_0(1-\bar{\chi}t)(1-\bar{\mu}t)$, and that of the scattered X-rays after absorption is $I_0\bar{\chi}t(1-\bar{\mu}t)$. Because $\bar{\chi}t$ and $\bar{\mu}t$ are small quantities compared with unity, the more general DEI equation can be expressed as

$$I = I_0(1-\bar{\mu}t-\bar{\chi}t)R(\theta_A+\theta_m)+I_0\bar{\chi}t\frac{\theta_D}{2\omega_S} \qquad (8)$$

Comparing Eq. (8) with Eq. (1), $I_R = I_0(1-\bar{\mu}t-\bar{\chi}t)$, and Chapman[6] neglected the part of small angle scattering reflected by the analyzer.

3 Six kinds of images in DEI

In DEI many different images can be obtained by adjusting the setting angle θ_A of the analyzer at different angles, but among these setting angles three angles, i.e. $\theta_A=0$, $\theta_A=-\theta_D/2$ and $\theta_A=\theta_D/2$ are mostly used, resulting in three typical kinds of images, namely the peak image (meaning at the peak of the rocking curve)

$$I_P = I_0(1-\bar{\mu}t-\bar{\chi}t)R(\theta_m)+I_0\bar{\chi}t\frac{\theta_D}{2\omega_S}, \qquad (9)$$

the low angle image

$$I_L = I_0(1-\bar{\mu}t-\bar{\chi}t)R\left(-\frac{\theta_D}{2}+\theta_m\right)+I_0\bar{\chi}t\frac{\theta_D}{2\omega_S}, \qquad (10)$$

and the high angle image

$$I_H = I_0(1-\bar{\mu}t-\bar{\chi}t)R\left(\frac{\theta_D}{2}+\theta_m\right)+I_0\bar{\chi}t\frac{\theta_D}{2\omega_S}. \qquad (11)$$

The rocking curves for the three typical images are shown in Fig.8 respectively.

From the low angle image and the high angle image three resultant images can be obtained, such as the adding image (this image was also named as the apparent absorption image by Chapman[6]):

$$\begin{aligned} I_{add} &= I_L + I_H \\ &= I_0(1-\bar{\mu}t-\bar{\chi}t)\left[R\left(-\frac{\theta_D}{2}+\theta_m\right)+R\left(-\frac{\theta_D}{2}+\theta_m\right)\right]+ \\ &\quad I_0\bar{\chi}t\frac{\theta_D}{\omega_S}, \end{aligned} \qquad (12)$$

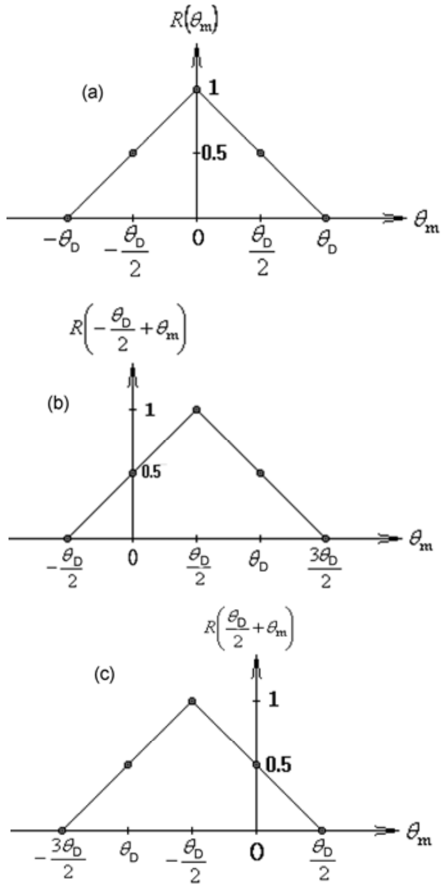

Fig.8 The rocking curves for (a) peak image, (b) low angle image, and (c) high angle image.

the subtracting image:

$$
\begin{aligned}
I_{\mathrm{sub}} &= I_{\mathrm{L}} + I_{\mathrm{H}} \\
&= I_0\left(1-\bar{\mu}t-\bar{\chi}t\right)\left[R\left(-\frac{\theta_{\mathrm{D}}}{2}+\theta_{\mathrm{m}}\right)-R\left(-\frac{\theta_{\mathrm{D}}}{2}+\theta_{\mathrm{m}}\right)\right],
\end{aligned}
\tag{13}
$$

and the refraction image (named by Chapman[6] on the condition that the refraction angle is within the region $(-\theta_{\mathrm{D}}/2,\ \theta_{\mathrm{D}}/2)$):

$$
\begin{aligned}
\theta_{\mathrm{m}} &= \left(\frac{\theta_{\mathrm{D}}}{2}\right)\frac{I_{\mathrm{L}}-I_{\mathrm{H}}}{I_{\mathrm{L}}+I_{\mathrm{H}}} \\
&= \left(\frac{\theta_{\mathrm{D}}}{2}\right)\frac{\left[R\left(-\frac{\theta_{\mathrm{D}}}{2}+\theta_{\mathrm{m}}\right)-R\left(-\frac{\theta_{\mathrm{D}}}{2}+\theta_{\mathrm{m}}\right)\right]}{\left[R\left(-\frac{\theta_{\mathrm{D}}}{2}+\theta_{\mathrm{m}}\right)+R\left(-\frac{\theta_{\mathrm{D}}}{2}+\theta_{\mathrm{m}}\right)\right]+\frac{\bar{\chi}t}{1-\bar{\mu}t-\bar{\chi}t}\left(\frac{\theta_{\mathrm{D}}}{\omega_{\mathrm{S}}}\right)} \\
&\approx \left(\frac{\theta_{\mathrm{D}}}{2}\right)\frac{\left[R\left(-\frac{\theta_{\mathrm{D}}}{2}+\theta_{\mathrm{m}}\right)-R\left(-\frac{\theta_{\mathrm{D}}}{2}+\theta_{\mathrm{m}}\right)\right]}{\left[R\left(-\frac{\theta_{\mathrm{D}}}{2}+\theta_{\mathrm{m}}\right)+R\left(-\frac{\theta_{\mathrm{D}}}{2}+\theta_{\mathrm{m}}\right)\right]}
\end{aligned}
\tag{14}
$$

where $\frac{\bar{\chi}t}{1-\bar{\mu}t-\bar{\chi}t}\left(\frac{\theta_{\mathrm{D}}}{\omega_{\mathrm{S}}}\right)$ in the denominator is a very small quantity and can be neglected. Three different combinations of two rocking curves for the three resultant images are shown in Fig.9 respectively.

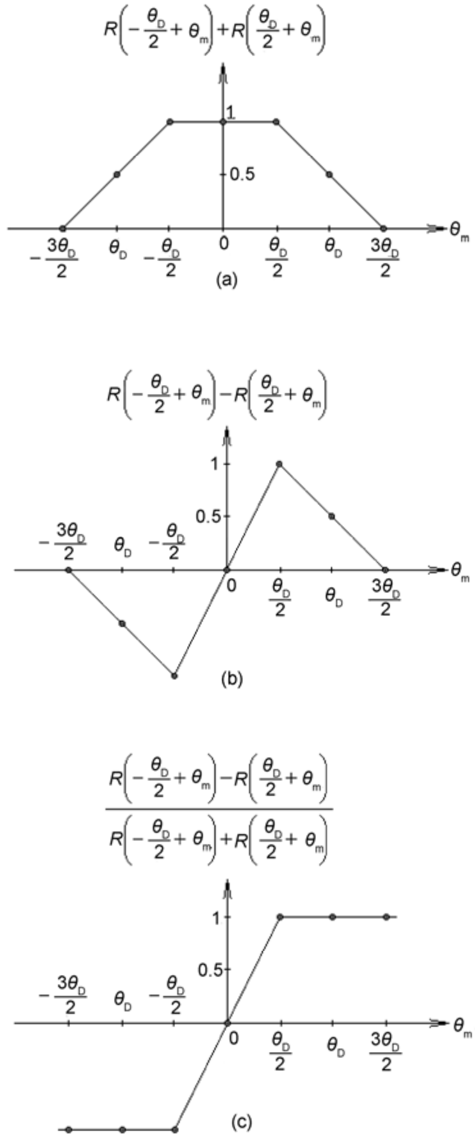

Fig.9 (a) Adding image curve, (b) subtracting image curve, and (c) refraction image curve. If the actual rocking curve instead of triangle-like curve is used, the refraction image curve will converge to zero at a large refraction angle.

4 Two comparisons among images

Both the peak image and adding image are absorption-like images, but the peak image gets higher contrast and resolution than the adding image does. On comparing Eqs. (9) and (12), two reasons were found as to why the peak image can get higher contrast and resolution. Both the peak image and the adding image have factor of $\left(1-\bar{\mu}t-\bar{\chi}t\right)$, as if they had the same extinction contrast apparently, but paying attention to the second terms on the right side in Eqs. (9) and (12), it was found that the acceptance of the adding image for small angle scattering is $2\theta_{\rm D}$ which is twice that of the peak image, resulting in lager point spread and higher background. The other cause comes from refraction. Comparing Figs. 8 (a) and 9(a), it was found that more refraction intensity is rejected in the peak image than in the adding image, resulting in sharper border in the peak image than in the adding image. That is to say the peak image gets higher contrast and resolution than the adding image does, because more small angle scattering and refraction intensity are rejected. Fig. 10 shows the comparison between the peak image and the adding image.

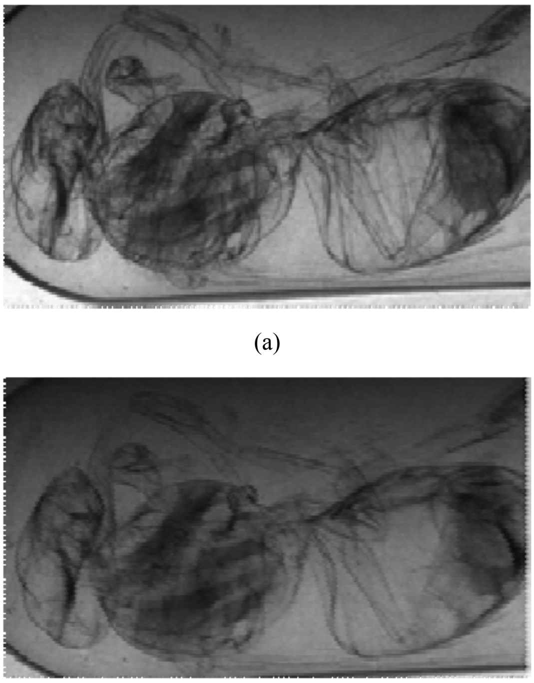

(a)

(b)

Fig.10 (a) The peak image and (b) the adding image of a bee.

Both the subtracting image and the refraction image can give information regarding refraction angle, but the refraction image gets higher contrast than the subtracting image does. Comparing Fig. 9 (b) and (c), it was found that both the subtracting image and the refraction image have the same refraction contrast when the refraction angle is within the region $(-\theta_{\rm D}/2,\ \theta_{\rm D}/2)$, but the refraction image gets higher contrast when the refraction angle is out of the region $(-\theta_{\rm D}/2,\ \theta_{\rm D}/2)$, resulting in sharper border in the refraction image than in the subtracting image. Fig. 11 shows the comparison between the subtracting image and the refraction image.

5 The more precise DEI equation

When the absorption and rejection of small angle scattering are not in small quantities, the more precise DEI equation becomes[12,13]:

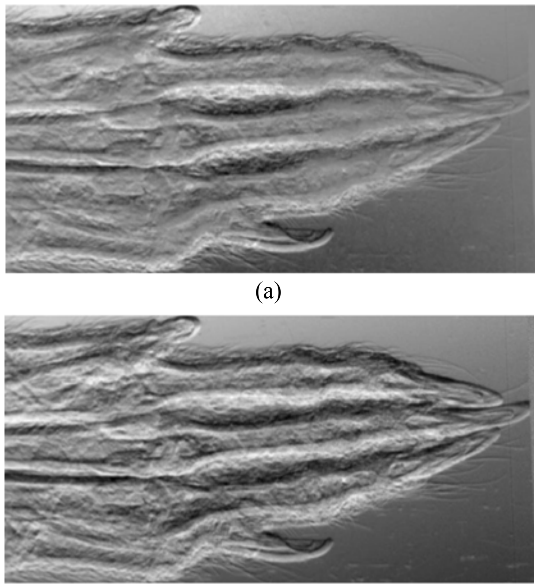

(a)

(b)

Fig.11 (a) The subtracting image and (b) the refraction image of a mouse paw.

$$I = I_0 \exp\left(-\bar{\mu}t-\bar{\chi}t\right)R\left(\theta_{\rm A}+\theta_{\rm m}\right)+ I_0\frac{\theta_{\rm D}}{2\omega_{\rm S}}\exp\left(-\bar{\mu}t\right)\left[1-\exp\left(-\bar{\chi}t\right)\right] \tag{15}$$

When DEI is considered to combine with computed tomography, the DEI equation can be written as:

$$I(x,y) = I_0\left[-\int_0^t \mu(x',y',z'){\rm d}z-\int_0^t \chi(x',y',z'){\rm d}z-\right]\times R\left[\theta_A+\int_0^t \frac{\partial n(x',y',z')}{\partial y}{\rm d}z\right]+ I_0\frac{\theta_D}{2\omega_{\rm S}}\exp\left(-\bar{\mu}t\right)\left[1-\exp\left(-\bar{\chi}t\right)\right] \tag{16}$$

where (x,y,z) and (x',y',z') denote the reference frame in the Lab and that fixed on the sample. The DEI equation used in computed tomography in practice is

$$I(x,y)=I_0\left[-\int_0^t \mu(x',y',z')\mathrm{d}z-\int_0^t \chi(x',y',z')\mathrm{d}z-\right]\times R\left[\theta_A+\int_0^t \frac{\partial n(x',y',z')}{\partial y}\mathrm{d}z\right] \quad (17)$$

and the second term on the right of Eq. (16) is treated as the noise background.

Part II. Computed tomography based on the DEI method

1 Introduction

Despite the higher contrast and resolution than the conventional X-ray projection imaging, DEI is still a 2-D imaging and all the structures overlap so that it is hard to determine the precise volumetric location of details inside the sample object. An efficient way to overcome this problem is to combine the DEI method using a CT scan methodology to collect real volumetric data, a method that is known as DEI-CT.

2 Possibilities of computed tomography based on the DEI method

The basis of conventional tomography in physics is Beer's law

$$I(x,y)=I_0\exp\left(-\int_0^t \mu(x',y',z')\mathrm{d}z\right) \quad (18)$$

and the basis in mathematics is Radon transformation. From Eqs. (2), (3) and (4) in Part I, three interactions in DEI can be written as three integrals, they are the integral of the absorption coefficient, the integral of the extinction coefficient, and the integral of derivative of the refractive index, respectively. If one of these three integrals can be written in the form similar to Beer's law, then the integrand can be reconstructed by using the algorithm based on Radon transformation. The possibility of combining the peak imaging with computed tomography is first investigated, followed by the investigation of the possibility of combining the refraction imaging with computed tomography.

3 DEPI-CT

The peak imaging equation is rewritten according to Eq. (17) as:

$$I_P(x,y)\approx\exp\left\{-\int_0^t\left\lfloor\mu(x',y',z')+\chi(x',y',z')\right\rfloor\mathrm{d}z\right\}\times R\left[\theta_m(x,y)\right] \quad (19)$$

If the refraction angles are assumed to be very small, Eq. (19) becomes

$$I_P(x,y)\approx I_0\times \exp\left\{-\int_0^t\left[\mu(x',y',z')+\chi(x',y',z')\right]\mathrm{d}z\right\} \quad (20)$$

As Eq. (20) is about the same as Beer's law, the integrand $\left[\mu(x,y,z)+\chi(x,y,z)\right]$ can be reconstructed by using conventional CT algorithm based on Radon transformation. Though the assumption is of something the matter, it is the point for us to start our DEI-CT theoretical and experimental research.

If the refraction angles are not very small, the logarithm of Eq. (19) is

$$\ln\left[\frac{I_0}{I_\mathrm{P}(x,y)}\right]=\int_0^t\left[\mu(x',y',z')+\chi(x',y',z')\right]\mathrm{d}z-\ln R\left[\theta_\mathrm{m}(x,y)\right] \quad (21)$$

The first term on the right side of the above-mentioned equation is nothing but Beer's law, and the second term is the contribution induced by the refraction angle. In general the refraction angles are very small and can be neglected, but on the border of the sample, the refraction angle may be larger than Darwin width, the reflectivity of the refraction beam will approximate to zero, i.e. $\ln R\left[\theta_\mathrm{m}(x,y)\right]\to\infty$, resulting in a very strong contour contrast on the border of the sample. This kind of contour contrast has been represented with mathematics, and certain complicated problems need to be investigated.

Fig. 12 shows the first result of the diffraction peak imaging computed tomography (DEPI-CT). The raw data were colleted by a graduate student, ZHENG Xin, and first slice images were reconstructed by another graduate student, WANG Junyue. And the volume rendering was reconstructed from the same data by a female graduate student, SHU Hang, as shown in Fig.13.

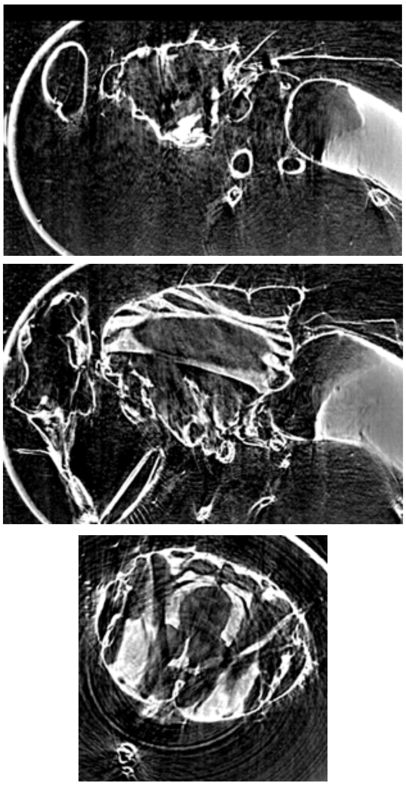

Fig.12 The slice images of a fly in different section plane.

Fig.13 The volume rendering of the same sample as in Fig.12.

4 Refraction CT based on DEI set-up

In the CT data acquisition process, the sample is rotated to obtain the projected images of the object using a detector, while for slice image reconstruction these projected images are back-projected along their own original projection directions after being treated using the same filtered function[14]. From the CT principle, two conditions have to be fulfilled, i.e., the projection of the function in the sample may be written as a line integral and the integrand at any point should be rotational invariable In X-ray projection imaging there are five imaging contrast forming mechanisms, which are the absorption contrast in conventional radiography, the phase contrast obtained with X-ray interferometer, the extinction contrast induced by the rejection of the small angle scattering, the phase gradient contrast (i.e., the refraction contrast) in DEI, and the contrast induced by the phase Laplacian term in the in-line phase contrast imaging (also called *phase propagation imaging*). All five imaging contrast forming mechanisms have been already used in CT method[15-20], however, there is no detailed theoretical study to check the rotation invariance of the functions to be reconstructed. Each of the functions, such as the linear absorption coefficient, the linear extinction coefficient, the phase, the phase gradient, and the phase Laplacian, can be written as a line integral and are relevant for the image reconstruction. However, in this article, only the phase gradient contribution is discussed, which is one of the main contributions to DEI-CT imaging.

In general, the relation[21] between the phase gradient and the gradient of refractive index is

$$(\frac{\lambda}{2\pi})\frac{\mathrm{d}}{\mathrm{d}s}\nabla\Phi(x,y,z)=\nabla n(x,y,z) \tag{22}$$

where s denotes the position along the path of X-ray beam. When the X-ray beam goes along Z axis, the sample can be described with limitary functions, and the phase gradient is small, so three integrals corresponding to the three components of the gradient of refractive index are obtained:

$$\theta_x=\int_{\text{sample}}\frac{\partial n(x,y,z)}{\partial x}\mathrm{d}z \tag{23}$$

$$\theta_y=\int_{\text{sample}}\frac{\partial n(x,y,z)}{\partial y}\mathrm{d}z \tag{24}$$

and

$$0=\int_{\text{sample}}\frac{\partial n(x,y,z)}{\partial z}\mathrm{d}z \tag{25}$$

where θ_x and θ_y denote the refraction angles in X-Z and Y-Z planes respectively. In Fig. 14, two different DEI-CT setups are shown, one shown in Fig.

14(a) using the conventional algorithm to reconstruct slice images because $\partial n(x,y,z)/\partial y$ is a rotational invariable, while the $\partial n(x,y,z)/\partial x$ contribution cannot be collected because of the crystal properties. On the contrary, in the second experimental setup shown in Fig. 14(b), only the $\partial n(x,y,z)/\partial x$ contribution plays the major role in DEI-CT.

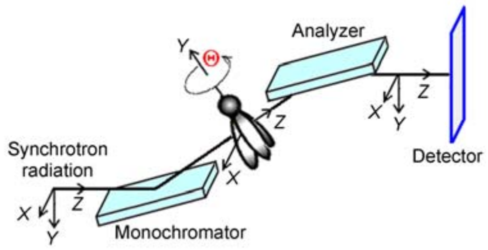

(a)

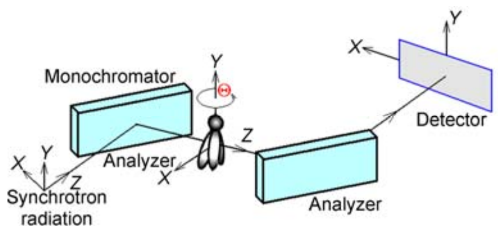

(b)

Fig.14 Two experimental setups: (a) with rotation axis of sample being perpendicular to that of the analyzer; (b) with rotation axis of sample being parallel to that of the analyzer.

On the condition that the refraction angle is within the region $(-\theta_D/2,\ \theta_D/2)$, θ_y in Fig. 14(a) and θ_x in Fig. 14(b) can respectively be expressed with the experimental data as

$$\theta_y = \left(\frac{\theta_D}{2}\right)\frac{I_L^{\perp} - I_H^{\perp}}{I_L^{\perp} + I_H^{\perp}} \tag{26}$$

And

$$\theta_x = \left(\frac{\theta_D}{2}\right)\frac{I_L^{//} - I_H^{//}}{I_L^{//} + I_H^{//}} \tag{27}$$

where superscripts $\perp$ and // denote the rotation axis of sample perpendicular to and parallel to that of the analyzer respectively. As shown in Fig. 14, we set the Y axis as the rotation axis of the sample, so that $\partial n(x,y,z)/\partial y$ in Fig. 14(a) is a rotational invariable; on the contrary, the behavior of $\partial n(x,y,z)/\partial x$ in Fig. 14(b) has to be treated carefully because it may be not constant under rotation. As a consequence, a new CT algorithm[22,23] based on the layout of Fig. 14(b) is presented and discussed. According to Fig. 15, when the X-ray beam propagates along the Z axis, and when the rotation angle of the sample $\Theta = 0$, according to Eqs.(23) and (25), the following equations can be obtained:

$$\theta_x = \int_{\text{sample}} \frac{\partial n(x,y,z)}{\partial x}\text{d}z = \int_{\text{sample}} |\nabla n|\sin\phi\,\text{d}z \tag{28}$$

and

$$0 = \int_{\text{sample}} \frac{\partial n(x,y,z)}{\partial z}\text{d}z = \int_{\text{sample}} |\nabla n|\cos\phi\,\text{d}z \tag{29}$$

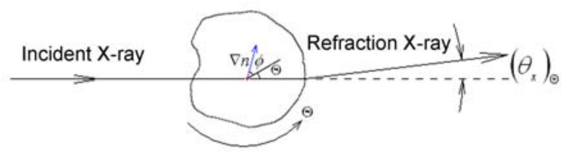

Fig.15 Scheme of the refracted X-rays emerging from the sample when the latter is rotated by Θ along an axis perpendicular to the paper.

Combining Eqs. (28) and (29),

$$\text{i}\theta_x = \int_{\text{sample}} |\nabla n|\exp(\text{i}\phi)\text{d}z \tag{30}$$

In the layout shown in Fig. 14(b), when the sample is rotated along the axis perpendicular to the foil $\Theta \neq 0$, three similar equations can be written as

$$(\theta_x)_\Theta = \int_{\text{sample}} |\nabla n|\sin(\phi+\Theta)\text{d}z \tag{31}$$

$$0 = \int_{\text{sample}} |\nabla n|\cos(\phi+\Theta)\text{d}z \tag{32}$$

and

$$\text{i}(\theta_x)_\Theta = \int_{\text{sample}} |\nabla n|\exp[\text{i}(\phi+\Theta)]\text{d}z \tag{33}$$

Eq. (33) can be rewritten as

$$\text{i}(\theta_x)_\Theta\exp(-\text{i}\Theta) = \int_{\text{sample}} |\nabla n|\exp(\text{i}\phi)\text{d}z = \int_{\text{sample}}\left[\frac{\partial n(x',y',z')}{\partial z'} + \text{i}\frac{\partial n(x',y',z')}{\partial x'}\right]\text{d}z \tag{34}$$

where $|\nabla n|\exp(\text{i}\phi) = \dfrac{\partial n(x',y',z')}{\partial z'} + \text{i}\dfrac{\partial n(x',y',z')}{\partial x'}$ is a rotational invariable. Eq. (34) is similar to Eq. (2) described in Ref. [19] except the factor of imaginary number. Combining Eqs. (24) and (26), [17]

$$\left[\theta_y(x,y)\right]_\Theta = \left[(\frac{\theta_D}{2})\frac{I_L^{\perp}(x,y)-I_H^{\perp}(x,y)}{I_L^{\perp}(x,y)+I_H^{\perp}(x,y)}\right]_\Theta = \int_0^t \frac{\partial n(x',y',z')}{\partial y'}\mathrm{d}z \tag{35}$$

Combining Eqs. (27) and (34),

$$\left[\theta_x(x,y)\right]_\Theta \cos\Theta = \left[(\frac{\theta_D}{2})\frac{I_L^{//}(x,y)-I_H^{//}(x,y)}{I_L^{//}(x,y)+I_H^{//}(x,y)}\right]_\Theta \cos\Theta = \int_{\text{sample}} \frac{\partial n(x',y',z')}{\partial x'}\mathrm{d}z \tag{36}$$

$$\left[\theta_x(x,y)\right]_\Theta \sin\Theta = \left[(\frac{\theta_D}{2})\frac{I_L^{//}(x,y)-I_H^{//}(x,y)}{I_L^{//}(x,y)+I_H^{//}(x,y)}\right]_\Theta \sin\Theta = \int_{\text{sample}} \frac{\partial n(x',y',z')}{\partial z'}\mathrm{d}z \tag{37}$$

Using Eqs. (35), (36) and (37) we can use the conventional algorithm to reconstruct slice images of three components of the gradient of refractive index. Fig.16 shows two reconstructed images of the component along Y axis of the gradient of refractive index, the sample is a quarter of an epoxy cylinder within which there are air bubbles with diameters of about 10~500 μm. The experimental data were acquired and the 3-d reconstructions were made by a graduate student, YU Jian.

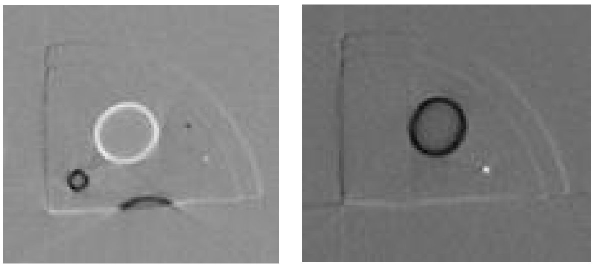

(a) (b)

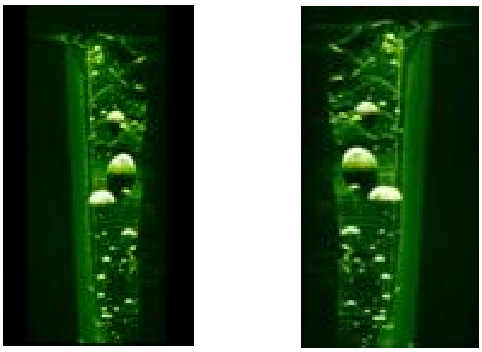

(c) (d)

Fig.16 (a) and (b) are two reconstructed slice images of the component along Y axis of gradient of refractive index; (c) and (d) are the three dimensional reconstructed images.

Fig. 17 shows two reconstructed images of the component along X axis and Z axis of the gradient of refractive index respectively of the same sample as in Fig.16. The experimental data were acquired and the slice images were reconstructed by WANG Junyue.

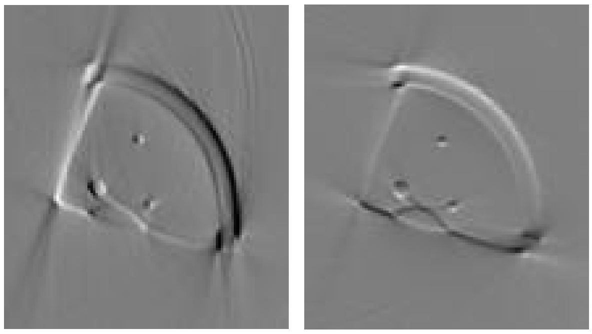

Fig.17 (a) and (b) are two reconstructed slice images of components along X axis and Z axis of the gradient of refractive index respectively.

5 Discussion

In this article, four new CT formulae based on the DEI method have been discussed, i.e. Eqs. (21), (35), (36) and (37). They lay a foundation for the method to combine DEI with a CT scan technique to collect real volumetric data.

Eq. (21) is the formula of DEPI-CT and partly related with phase contrast. When the refraction angles are very small, that is, smaller than the Darwin width of the analyzer, the second term on the right of Eq. (21) can be neglected and the formula is nearly the same as Beer's law. By using the algorithm based on Radon transform, the distribution of $\mu(x,y,z)+\chi(x,y,z)$ in the sample can be reconstructed. On the other hand, when the refraction angles are not very small, that is larger than the Darwin width of the analyzer when X-rays graze the border of the sample, the second term on the right of Eq. (21) will approach to infinity, and the reconstructed image is the combination of the distribution of $\mu(x,y,z)+\chi(x,y,z)$ with much stronger contour contrast of the sample by using the back-project algorithm. In this case the second term $\ln R\left[\theta_m(x,y)\right]$ in Eq. (21) can not be written as a line integral, and does not fulfill the condition of rotation invariance, but this case only takes place when X-rays graze the border or the interface of the sample and give the strongest contrast.

A similar thing also happens in the pure refraction CT when the refraction angles are larger than the Darwin width. In this case larger refraction angle cannot further result in larger intensity on the detector, and Eqs. (35), (36) and (37) are no longer tenable, that is to say the reconstructed images of the components of the gradient of refractive index cannot give the right values on the border of the sample.

Though the function describing the border or interface of the sample cannot be written as a line integral and may not be a rotation invariable, and the requirements of Radon transformation cannot be fulfilled, the reconstruction based on data collected by the DEI method by using the filtered back-project algorithm can in fact give much better images of the sample with higher resolution and contrast in comparison with the conventional CT method.

As a matter of fact the Beer's law is an ideal case, in the data acquisition process of conventional CT, the refraction, elastic scattering, inelastic scattering and beam hardening will debase the data quality. All these effects do not fulfill the requirements of Radon transformation because they are not rotation invariables and even cannot be written as a line integral in general. Researchers have been dedicating themselves to solve these problems, and many patents related with these problems were produced.

On comparing with conventional CT, on the one hand DEI-CT can get much better slice image and volume rendering of the sample, on the other hand the imaging mechanisms and artifacts problems in DEI-CT need further investigating.

Conclusions for two parts of this article

In Part I, DEI is regarded as the development from pinhole imaging and conventional X-ray project imaging, and the more general DEI equation is derived using simple concepts. Not only does the new DEI equation explain all the problems that can be explained with former DEI equation proposed by Chapman, but also explains the problems that cannot be explained with the former DEI equation, such as the noise background caused by the small angle scattering reflected by the analyzer.

In Part II, the DEPI-CT formula is proposed and the contour contrast caused by extinction of the refraction beam is qualitatively explained; and then based on the work of Ando's group[19] two formulae of the refraction CT with the DEI method were proposed. Combining one refraction CT formula[17] formerly proposed with the two refraction CT formulae proposed here, the whole framework of CT algorithm can be made to reconstruct three components of the gradient of refractive index.

References

1 Ando M., Hosoya S., in Proceeding of 6th International Conference on X-ray Optics and Microanalysis (edited by Shinoda G., Kohra K., Ichinokawa T.) University of Tokyo Press, Tokyo, 1972:63.

2 Davis T.J., Gao D., Gureyev T.E., *et al*. Nature, 1995, **373**:595.

3 Snigirev A., Snigireva I., Kohn V., *et al*. Rev. Sci. Instrum. 1995, **66**:5486.

4 Wilkins S. W., Gureyev T. Ei., Gao D., *et al*. Nature, 1996, **384**:335.

5 Margaritondo G., Tromba G., J. Appl. Phys. 1999, **85**:3406

6 Chapman L.D., Thomlinson W.C., Johnston R.E., *et al*. Phys. Med. Biol. 1997, **42**:2015.

7 Hwu Y., Hsieh H., Lu M. *et al*. J. Appl. Phys. 1999, **86**:4613.

8 Oltulu O., Zhong Z., Hasnah M., *et al*. J.Phys.D: Appl. Phys. 2003, **36**:2152

9 Kiss1 M., Sayers1 D., Zhong Z., Phys. Med. Biol. 2003, **48**:325

10 James R.W. The optical principles of the diffraction of X-rays, Ox Bow Press, 1982.

11 Zhu P., Yuan Q., Huang W., *et al*. J. Phys. D Appl. Phys, 2006, **39**:4142.

12 Zhu P., Wang J., Yuan Q., *et al*. Proc. 8th Int. Conf. X-ray Microscopy (invited talk), IPAP Conf. Series 7, 407-410 (2006).

13 Zhu Peiping, Yuan Qingxi, Huang Wanxia, *et al*. Physica Sinica (in Chinese), 2006, **55**:1089.

14 Macovski A., Medical Imaging Systems, Prentice–Hall, Englewood Cliffs, New Jersey, 1983.

15 Momose A., Takeda T., Itai Y. *et al*. Nature Medicine, 1996, **2**:473.

16 Cloetens P., Ludwig W., Baruchel J., Appl. Phys. Lett., 1999, **75**:2912.

17 Dilmanian F. A., Zhong Z., Ren B.,*et al*. Phys. Med. Biol. 2000, **45**:933.

18 Fiedler S., Bravin A., Keyrilainen J., *et al*. Phys. Med. Biol. 2004, **49**:175.

19 Msksimenko A., Ando M., Hiroshi S. *et al*. Appl. Phys. Lett. 2005, **86**:124105.

20 Yuan Q., Wang J., Zhu P., *et al*. High Energy Phys. Nucl. Phys. (in Chinese), 2005, **29**:1023.

21 Born M., Wolf E., The Principle of optics, Pergamon Press, 1975.

22 Zhu P., Wang J., Yuan Q., *et al*. Appl. Phys. Lett. 2005, **87**:264101.

23 Wang J., Zhu P., Yuan Q.,*et al*. Phys. Med. Biol. 2006, **51**:3391-3396.